Title

A Prototype High-Resolution Small-Animal PET Scanner Dedicated to Mouse Brain Imaging

Authors

Yang, Yongfeng
Bec, Julien
Zhou, Jian
et al.

Peer reviewed

A high resolution prototype small-animal PET scanner dedicated to mouse brain imaging

Yongfeng Yang[1,2], **Julien Bec**[1], **Jian Zhou**[1], **Mengxi Zhang**[1], **Martin S Judenhofer**[1], **Xiaowei Bai**[1], **Kun Di**[1], **Yibao Wu**[1], **Mercedes Rodriguez**[1,3], **Purushottam Dokhale**[4], **Kanai S. Shah**[4], **Richard Farrell**[4], **Jinyi Qi**[1], and **Simon R. Cherry**[1]

[1]Department of Biomedical Engineering, University of California-Davis, One Shields Avenue, CA 95616, USA

[2]Shenzhen Institutes of Advanced Technology, Chinese Academy of Sciences, Shenzhen 518055, China

[3]Instituto de Física, Universidad Nacional Autónoma de México, A. P. 20-364, 01000 Mexico D. F., Mexico

[4]Radiation Monitoring Devices Inc., Watertown, MA 02172, USA

Abstract

A prototype small-animal PET scanner was developed based on depth-encoding detectors using dual-ended readout of very small scintillator elements to produce high and uniform spatial resolution suitable for imaging the mouse brain.

Methods—The scanner consists of 16 tapered dual-ended readout detectors arranged in a ring of diameter 61 mm. The axial field of view is 7 mm and the transaxial field of view is 30 mm. The scintillator arrays consist of 14×14 lutetium oxyorthosilicate (LSO) elements, with a crystal size of 0.43×0.43 mm^2 at the front end and 0.80×0.43 mm^2 at the back end, and the crystal elements are 13 mm long. The arrays are read out by 8×8 mm^2 and a 13×8 mm^2 position-sensitive avalanche photodiodes (PSAPDs) placed at opposite ends of the array. Standard nuclear instrumentation module (NIM) electronics and a custom designed multiplexer are used for signal processing.

Results—The detector performance was measured and all except the very edge crystals could be clearly resolved. The average detector intrinsic spatial resolution in the axial direction was 0.61 mm. A depth of interaction resolution of 1.7 mm was achieved. The sensitivity of the scanner at center of the field of view was 1.02% for a lower energy threshold of 150 keV and 0.68% for a lower energy threshold of 250 keV. The spatial resolution within a field of view that can accommodate the entire mouse brain was ~0.6 mm using a 3D Maximum Likelihood-Expectation Maximization (ML-EM) reconstruction algorithm. Images of a micro hot-rod phantom showed that rods with diameter down to 0.5 mm could be resolved. First *in vivo* studies were obtained

For correspondence or reprints contact: Yongfeng Yang, Shenzhen Institutes of Advanced Technology, Chinese Academy of Sciences, Shenzhen 518055, China, yf.yang@siat.ac.cn, Tel: 86-755-86392256, Fax: 86-75586392299.
The first author is not currently in training.

Disclaimer: No

using ^{18}F-fluoride and confirmed that 0.6 mm resolution can be achieved in the mouse head *in vivo*. Brain imaging studies with ^{18}F-fluorodeoxyglucose were also acquired.

Conclusion—A prototype PET scanner achieving a spatial resolution approaching the physical limits for a small-bore PET scanner set by positron range and acolinearity was developed. Future plans are to add more detector rings to extend the axial field of view of the scanner and increase sensitivity.

Keywords

Positron emission tomography; small animal PET; high resolution; mouse; brain imaging

1. INTRODUCTION

Currently, the spatial resolution of most dedicated small-animal PET scanners is only 1–2 mm (1–4). Mice are the most frequently used animals for animal model studies of human diseases. The strengths of the mouse as an experimental model include the fact that roughly 95% of its genes have a human homologue, techniques for genetic manipulation are mature, the time to reach breeding age is short (speeding up the development of transgenic/knockout animals), and housing/breeding costs are relatively low. The dimension of a mouse brain (~1.5 cm) is about one tenth that of the human brain (~15 cm). A spatial resolution of ~0.5 mm is required for a small-animal PET scanner if one wants to image the mouse with the same relative spatial resolution as achieved in a human using a clinical whole body PET scanner with 5-mm spatial resolution (5, 6). It is almost impossible to achieve the same relative spatial resolution (~0.2 mm) for a mouse brain as the human brain imaged with a dedicated brain PET scanner that achieves ~2 mm spatial resolution (7), due to the fundamental physics limits of the signal generation mechanism (8).

High spatial resolution is required to visualize the distribution of the radiotracer within small brain regions and to improve quantification of the tracer by reducing the partial volume effect. Improving spatial resolution has been a major focus in small-animal PET instrumentation (9–13). The spatial resolution of a PET scanner is limited by the crystal size, positron range, acollinearity, depth of interaction (DOI), crystal encoding, sampling non uniformity and image reconstruction (14). In this work we focus on developing a high resolution prototype small-animal PET scanner with spatial resolution approaching the physical limits of a preclinical PET scanner by minimizing the contribution from each of the above factors. We use depth-encoding detectors based on dual-ended readout of finely pixelated LSO arrays with PSAPDs (15–17). We have previously shown similar detectors could resolve crystals as small as 0.5 mm and provide a DOI resolution of 2 mm (16). The contributions from crystal size, DOI and crystal encoding are reduced by using this detector design. Depth-encoding detectors can also reduce any resolution degradation or artifacts due to insufficient sampling since the sampling is improved using the DOI information. Using depth-encoding detectors with excellent DOI resolution, it is possible to design scanners with smaller detector ring diameter to reduce both scanner cost and the contribution of acolinearity, as well as to increase sensitivity. We also are developing an iterative reconstruction algorithm with accurate system modeling to reduce the contribution from image reconstruction.

The high resolution PET scanner we are developing is dedicated to mouse brain imaging since it is an application where very high spatial resolution is required while the cost of employing advanced high resolution detectors is manageable since the field of view requirement and therefore detector volume required for mouse brain imaging is relatively small. Initially, we have developed a one ring prototype PET scanner to test the detector approach and system concepts. In this paper we describe the design of the prototype scanner and demonstrate its spatial resolution and imaging performance.

2. MATERIALS AND METHODS

The prototype scanner

Sixteen tapered LSO arrays cut into 14×14 elements and 13 mm thick are used in the prototype scanner. The crystal size of the LSO arrays is 0.43×0.43 mm^2 at the front end and 0.80×0.43 mm^2 at the back end. Two of the four long crystal faces are polished, the other 4 crystal faces are left as unpolished and Toray lumirror E60 film (Toray Industries Inc., Japan) is used as an inter-crystal reflector. Details of the array fabrication have been published previously (15, 16). The arrays are read out by PSAPDs with active areas of 8×8 mm^2 and 13×8 mm^2 (18) placed at opposite ends of the array so that the DOI can be estimated. Figure 1 shows photographs of a LSO array and the two different-sized PSAPDs. The physical dimensions of the two PSAPDs are 10×11.5×1.4 mm^3 and 15.2×16.7×1.4 mm^3.

Figure 1 also shows a drawing of the detector arrangement in the prototype scanner and photographs of the completed scanner. The ring diameter of the scanner is 61 mm and the aperture of the scanner is 40 mm. The axial field of view is 7 mm and the transaxial field of view is 30 mm. The gap between the adjacent arrays is 5 mm. For scanners with such small crystal elements, high positioning accuracy is necessary for the crystal arrays to realize the full resolution potential. An aluminum ring support was designed to hold the arrays in known and precise locations. The performance of PSAPDs (e.g. signal to noise ratio and gain) changes with temperature (19), therefore the scanner gantry was cooled by an Air-Jet Crystal Cooler (FTS System, Inc., Stone Ridge, NY) to ensure a stable operating temperature. In order to obtain efficient and uniform cooling of all PSAPDs, the cold and dry air was sent into the Al support structure as well as distributed to the PSAPDs placed at both end of the crystal arrays. Computed fluid dynamics simulations were used to guide the cooling system design. These simulations showed that the variation of the cold air pressure across the locations of the 32 PSAPDs in the system were within 5% in the final cooling design selected. The space where all LSO arrays, PSAPDs and readout preamplifier boards reside also is cooled. An animal bed that can be moved in all three directions was also fabricated and integrated with the scanner.

The schematics of the electronics system for the prototype scanner are shown in Supplemental Figures 1 and 2. Standard NIM electronics were used for signal processing and a multiplexer (20) was also designed and used to decrease the number of energy signals from 128 (32 PSAPDs each with four signal outputs) to 16. The timing signals from the front and back PSAPDs were amplified by a CR-110 preamplifier (Cremat Inc., Boston), summed by using a linear fan in/out and then amplified by a timing filter amplifier before

being sent to a constant fraction discriminator (CFD). The CFD produced two logic signals, one was used for coincidence formation and the other one was sent to the multiplexer for detector identification number (ID) determination. The four energy signals of each PSAPD were also first amplified by CR-110 preamplifiers and then amplified by a 16 channel shaping amplifier. The 128 energy signals from the 32 PSAPDs, the 16 CFD signals and the coincidence event trigger signal were sent to the multiplexer. Whenever an event trigger occurs, the multiplexer determines the two coincidence detectors from the CFD signals. Then the 16 energy signals from the two detector modules are passed to two data acquisition boards, digitized and stored in as list mode data. The multiplexer also produces 8 logic signals (the first 4 signals for the first detector and the last 4 signals for the second detector) that are used to encode the detector pair IDs (detector ID run from 0 to 15). For example when detector ID is 0, all 4 logic signals are 0 V and when the detector ID is 15, all 4 signals are +5 V. The 8 logic signals were also digitized using one of the data acquisition boards and stored in the list mode data file (21).

Detector performance

The flood histogram, DOI resolution and energy resolution of one detector module were measured using the same experimental setup, data acquisition system and data analysis procedures as shown in our previous publications (15, 22). The experimental methods are briefly summarized below. Flood histograms and DOI responses of all 16 detectors were also measured within the scanner. For all measurements presented, the temperature was set to ~5°C.

1. Flood histograms and energy resolution—The measurements were performed in single modes with the array irradiated by a 0.3 mm diameter ^{22}Na point source placed 5 cm from one side of the array. To analyze the data, first a preliminary flood histogram (with low energy threshold) was obtained from the list mode data. From this, a crystal look-up table was generated. The list mode data were then reprocessed using the crystal look-up table to obtain crystal energy spectra for each crystal in an array. The photopeak amplitude and energy resolution of all crystals was obtained by Gaussian fitting of the energy spectra. In addition, the list mode data were re-analyzed using the crystal look-up table and crystal photopeak amplitude information to create flood histograms for a specific energy window.

2. DOI resolution—The measurements were performed in coincidence mode, using the same source and selectively irradiating at five depths of 1.5, 4, 6.5, 9 and 11.5 mm from the narrow end of the array using electronic collimation. Details of the experimental setup can be found in reference (15). The distance from the point source (0.3 mm in diameter) to the collimating slab detector (1.5 mm thick) was 6 cm and the distance from the point source to the LSO array was 4 cm. The radiation beam width on the array is estimated from the geometry to be ~1 mm. Histograms of the DOI ratio (ratio of the energy signal of one PSAPD to the sum of the energy signals of both PSAPDs) as a function of irradiation depth were obtained for the entire array and for individual crystals. The DOI resolution was calculated by a Gaussian fit of the DOI ratio histograms. The full width at half maximum (FWHM) DOI resolution was then converted to units of mm by a linear fit of the peak values

of the DOI ratio histogram of the entire array to the known depth of irradiation, using the data obtained at depths of 1.5 and 11.5 mm.

Scanner performance

1. Intrinsic spatial resolution—The intrinsic spatial resolution of the detectors after installation in the scanner was measured by moving a 0.3 mm diameter ^{22}Na point source along the central axis of the scanner in the axial direction with a step size of 0.1 mm. In total 36 positions in the center of axial field of view (FOV) were measured. For each position, the coincidence counts measured from each crystal in the two middle rows (crystal rows 7 and 8) in one detector with the corresponding crystal in the opposite detector were obtained using the crystal look up tables and a detector based lower energy threshold of 250 keV. The coincidence counts for the 14 crystal pairs in the same row were summed up to increase the statistics of the measurements. In total 16 curves of the coincidence counts versus source position (intrinsic spatial resolution profiles) were obtained (8 different detector module pairs × two rows of crystals). The FWHM of the profiles was obtained by using linear interpolation of the measured data. The measurements presented were not corrected for the 0.3 mm diameter of the point source.

2. Timing resolution—A uniform cylinder with a diameter of 30 mm and 10 mm in length (covering the whole field of view of the scanner) was filled with ^{18}F$^-$ and placed in the scanner. The logic OR of the eight detector timing signals was used as the start signal and the logic OR of the other eight timing signals was used as the stop signal that was fed into a time to digital converter. The measured timing spectrum was fit with a Gaussian function and the FWHM timing resolution of the scanner measured.

3. Sensitivity—The sensitivity of the scanner was measured by stepping a 0.3 mm ^{22}Na point source along the central axis of the scanner. The sensitivity for two different lower energy thresholds of 150 keV and 250 keV was measured. The 90.3% β^+ decay branching ratio for ^{22}Na was accounted for, however the small degree of attenuation of γ rays in the plastic disk containing the point source was not corrected for. The relative sensitivity change of the scanner for different coincidence timing windows was also measured by using the same uniform cylinder as the timing resolution measurement with a lower energy threshold of 150 keV. The width of the coincidence window to be used for later studies was determined based on this measurement.

4. DOI calibration—From a GATE simulation (23), the interaction probabilities of 511 γ rays along the depth of the tapered array used in the scanner were obtained for a point source at the center of the FOV (Supplemental Figure 3A). The curves of interaction probabilities vs. DOI ratio (DOI responses) were measured for all 16 detectors by placing a point source at the center of the FOV. Supplemental Figure 3B shows the measured DOI response for one detector. The DOI calibration curve of depth vs. DOI ratio can then be obtained by finding the values for the depth and DOI ratio that have the same fraction of counts under the curve. For one detector array, the depth vs. DOI ratio was actually measured (during the DOI resolution measurement). This represents the gold standard method. Supplemental Figure 3C shows the calibration curve of that detector obtained by the current method as compared

with the gold standard showing excellent agreement and validating this simple approach to DOI calibration. This method was therefore used for DOI calibration of all the detectors in the prototype scanner.

5. Image reconstruction—We use a sinogram-based 3D ML-EM reconstruction algorithm using 9 DOI bins. The size of the sinogram dataset was $71 \times 112 \times 9 \times 9 \times 14 \times 14$ (radial projection$\times$angle$\times$DOI$_1\times$DOI$_2\times$ring$_1\times$ring$_2$) elements. The system matrix was precomputed by dividing each depth encoding crystal into $5\times5\times11$ sub-elements to perform the numerical volume integration using Siddon's method (24). The system matrix was compressed with both axial and transaxial symmetries (25), and saved in sparse matrix format. An image domain point spread function was also included in the reconstruction. The point spread functions were obtained using a double Gaussian model estimated from reconstructed images of real point source scan data at different locations in the field of view (26). A uniform cylinder phantom filled with 5.5 MBq ^{18}F$^-$ was scanned for four hours (50 million counts) to obtain normalization data. The cylinder was 30 mm in diameter and 10 mm long, which covered the entire FOV of the scanner. Crystal efficiencies and geometric correction factors were estimated using an iterative based normalization algorithm (27). Random and scatter correction was not considered in the reconstruction. Each image was reconstructed into a matrix of $149\times149\times29$ voxels with a voxel size of $0.2\times0.2\times0.25$ mm^3.

6. Image spatial resolution—The spatial resolution was measured following the NEMA NU4 standard for small animal PET scanners (28). A 0.3 mm ^{22}Na point source was scanned at radial distances of 0, 5, 10 mm both at the center of the axial FOV and at an axial offset of 1.75 mm from the center. Sources were reconstructed (700 iterations) by adding a uniform warm background without noise to the sinogram to ensure the measured resolution is not artificially improved due to the non-negativity constraint in the ML-EM algorithm. In the reconstructed image, the intensity ratio of the point source to the background was 1:10. The background was subtracted from the reconstructed image. One dimensional profiles in all three directions were obtained through the point source images and FWHM image resolution was obtained by using a Gaussian fit to the profiles. A detector based lower energy threshold of 250 keV was used for this and all subsequent imaging studies. The crystal look-up tables of all detectors were created by using the flood histograms obtained from the normalization scan.

Phantom study

A micro hot rod phantom filled with ^{18}F$^-$ was scanned with both the prototype PET scanner and Siemens Inveon D-PET scanner (2). The rod diameters of the phantom are 0.35, 0.40, 0.45, 0.50, 0.60 and 0.75 mm, and the rod to rod distance is twice the rod diameter. For the prototype scanner, the scan time was 240 min and the activity at the start was 4.2 MBq. In total 38 million counts were acquired. For the D-PET scanner, the scan time was 30 min and the starting activity was 4.4 MBq. In total 380 million counts were acquired. A longer acquisition time was used for the prototype scanner as it only has one detector ring (therefore lower sensitivity) and sufficient counts are required to reconstruct at the highest possible resolution. The dataset from the prototype scanner was reconstructed by a 3D ML-EM algorithm with 700 iterations. The D-PET scanner images were reconstructed by 3D

ordered subset expectation maximization/maximum a posteriori (OSEM/MAP) with the default reconstruction parameters (2 OSEM iterations and 18 MAP iterations) suggested by the vendor.

In-vivo mouse brain studies

The prototype scanner has a small axial FOV of 7 mm and is designed primarily for mouse brain imaging. The activity outside of the FOV can contribute to singles, randoms and scatters. All *in-vivo* mouse brain studies were therefore performed by inserting the mouse body in a tungsten tube to shield activity outside the field of view. This tube was 60 mm long and had an inner diameter of 25 mm and outer diameter of 35 mm. The effectiveness and need for shielding was demonstrated by prior counting rate performance data obtained with and without lead shielding (see Supplemental Figure 4). The tungsten tube also served the purpose of maintaining animal temperature, as it was warmed by ultra-thin heating sheets to a temperature of 35°C to keep the mice warm during imaging.

Two animal scans were performed under approval from the UC Davis Institutional Animal Care and Use Committee. Mice were anesthetized with 1% isoflurane during intravenous injection and imaging, and were awake during the uptake time.

Study 1 – Bone Scan—A juvenile 12.6 g mouse was injected with 18 MBq $^{18}F^-$ and the head positioned for imaging mouse in the prototype scanner. The scan started 120 min after injection and lasted for 60 min. In total 6.2 M counts were acquired. To compare, an 11.9 g mouse was injected with 12 MBq $^{18}F^-$ and was scanned on the D-PET scanner with the mouse skull in the center of the axial FOV of the scanner. The scan was started 30 min after the injection and lasted for 30 min. In total 459 million counts were acquired. The image from the prototype scanner was reconstructed by a 3D ML-EM algorithm with 300 iterations and the image from the D-PET scanner was reconstructed by 3D OSEM/MAP.

Study 2 – ^{18}FDG Scan—A 19.4 g mouse was injected with 21 MBq of ^{18}F-fluorodeoxyglucose. The mouse brain was scanned on the D-PET scanner 30 min after the injection and the scan lasted for 15 min. In total 498 million counts were acquired. Then the mouse was moved to the prototype scanner for a 60 min scan starting 60 min after injection. In total 6.3 million counts were acquired. The image from the prototype scanner was reconstructed by a 3D ML-EM algorithm with 60 iterations and the image from the D-PET scanner was reconstructed by 3D OSEM/MAP.

3. RESULTS

Detector performance

Supplemental Figure 5 shows a representative flood histogram from one detector and the energy spectra of a center crystal and a crystal in the second row from the edge of the detector. The lower energy threshold was set at 250 keV for the events contributing to the flood histogram. All but the edge two rows of the crystals can be clearly resolved. The energy resolution of the center crystals ranges from 20 to 25%. For the two edge rows of the crystals, the energy resolution is degraded since crystals in the edge row and the second row

cannot be clearly resolved and the photopeak amplitude of crystals in the edge row is lower. Supplemental Figure 5 also shows the DOI responses of all crystals measured at five depths with electronic collimation (lower energy threshold also 250 keV). The average DOI resolution over the five depths was 1.7 mm. The estimated width of the collimated beam of ~1 mm was not subtracted from the results. The average DOI resolution obtained from the DOI responses of individual crystals was 1.5 mm. The measured flood histograms and DOI response of the 16 detectors inside the scanner showed only small variations among them (data not shown).

Scanner performance

Supplemental Figure 6 shows profiles of the intrinsic spatial resolution measurements for two middle rows of crystals (summed over the crystals in that row) from one pair of detectors. In total 16 profiles were obtained for 8 detector pairs. The average intrinsic spatial resolution of the 16 measured profiles was 0.61 mm, with a maximum of 0.68 mm and a minimum of 0.54 mm.

The scanner timing resolution was 40 ns. The poor timing resolution is mainly a result of the well-characterized position dependent time shift of PSAPDs (29–31). Supplemental Figure 7 shows the sensitivity of the scanner for different axial positions. The sensitivity at the center FOV was 1.02% and 0.68% for lower energy thresholds of 150 and 250 keV, respectively. Supplemental Figure 7 also shows the relative sensitivity measured with a uniform cylinder phantom for different coincidence timing windows. The lower energy threshold for this measurement was 150 keV. A coincidence timing window of 60 ns was used for all imaging studies based on this result.

Figure 2 shows reconstructed images of the point source measured at five positions within the scanner, both in the central axial slice, and in a slice corresponding to one-fourth of the axial FOV (1.75 mm from the center). Figure 2 also shows the measured spatial resolution. The reconstructed axial spatial resolution was ~0.45 mm, which is the best among all three directions since the crystal dimensions are not tapered in the axial direction. The radial and tangential spatial resolution was between 0.5 and 0.7 mm for all positions measured. The spatial resolution at a radial offset of 5 mm was the worst probably due to the fairly large gaps between the detector blocks. An average spatial resolution of 0.55 mm was achieved across a FOV that can accommodate the entire mouse brain.

Phantom and in-vivo animal studies

Figure 3 shows reconstructed images of the micro hot rod phantom measured with the prototype scanner and on a Siemens Inveon D-PET scanner. For images acquired with the prototype scanner, rods with diameter down to 0.5 mm can be resolved. Even the largest rods of 0.75 mm cannot be resolved in the images from the D-PET since it has a spatial resolution of ~ 1.5 mm (2).

Figure 4 shows images of ^{18}F-fluoride uptake in the head of two juvenile mice, one was scanned with the prototype scanner and the other was scanned with the D-PET. The D-PET images are 5 contiguous slices with a slice thickness of 0.80 mm. The slice thickness of the prototype scanner is 0.25 mm, and one in every three slices is shown. The images from the

prototype scanner showed much higher spatial resolution as expected. Profiles were also taken through the skull of the mice (estimated true thickness ~ 250 microns). The FWHM of the profiles measured with the prototype scanner was 0.6 mm and with the D-PET was 1.8 mm indicating that the high resolution measured in phantom studies also can be obtained in vivo.

Figure 5 shows FDG mouse brain images from the same mouse obtained from the prototype scanner and the D-PET scanner. The prototype PET scanner images show much higher spatial resolution and more detailed structure; however the noise level is clearly higher due to the limited counts (6.3 million events versus 498 million events for the D-PET scanner) that could be collected with this 1-ring prototype. In the future the sensitivity of the scanner needs to be significantly increased to take full advantage of the high spatial resolution.

4. DISCUSSION

A one detector ring prototype high-resolution small animal PET scanner was developed using dual-ended readout depth encoding tapered detectors. The very small crystal element size (0.43 mm at the front end), combined with a 3D ML-EM reconstruction algorithm that accurately models system geometry and other physical processes that impact the localization of the annihilation photons, led to a reconstructed spatial resolution that averaged 0.55 mm across a volume that can accommodate the mouse brain. Animal studies confirmed this resolution could be reached in vivo and demonstrate some of the highest resolution PET scans ever acquired in a living subject, approaching the limits dictated by positron physics and detector interaction physics (8).

While the spatial resolution performance is outstanding, and the approach taken here provides a platform for future development, this prototype has a number of significant limitations that must be overcome to produce a robust and high performance animal PET scanner. This prototype scanner only has one detector ring, leading to poor coverage (axial FOV of only 7 mm) and low sensitivity. Second, the timing resolution is poor (40 ns) due to the position-dependent timing shifts within the PSAPDs and the fact that the electronics used for this scanner cannot do crystal-by-crystal based timing corrections. Third, there are 5 mm gaps between the detector modules in the prototype scanner. The gaps reduce the solid angle coverage of detectors so the system sensitivity is reduced. In order to overcome these limitations, future development will focus on extending the crystal length (from 13 mm to ~20 mm), extending the axial FOV of the scanner by adding more detector rings, switching from PSAPDs to silicon photomultipliers to obtain far better timing resolution, and reducing the gaps between detector modules to 1 mm or less by careful design of the readout electronics (for example by using the flex readout boards) and using silicon photomultipliers with a through-silicon via and with minimal dead space.

5. CONCLUSION

In summary, this prototype scanner meets its design specification of achieving a spatial resolution approaching the limits for a small-bore PET scanner set by physics such as the positron range and acolinearity. Future development based on this approach should result in

a very high performance scanner that combines the high spatial resolution already demonstrated with high sensitivity and good count rate performance to produce a system appropriate for a broad array of applications in the biomedical sciences.

Supplementary Material

Refer to Web version on PubMed Central for supplementary material.

Acknowledgments

References

1. Goertzen AL, Bao QN, Bergeron M, et al. NEMA NU 4-2008 Comparison of preclinical PET imaging systems. Journal of Nuclear Medicine. 2012; 53:1300–1309. [PubMed: 22699999]

2. Bao Q, Newport D. Chen M, Stout DB, Chatziioannou AF. Performance evaluation of the Inveon dedicated PET preclinical tomograph based on the NEMA NU-4 standards. Journal of Nuclear Medicine. 2009; 50:401–408. [PubMed: 19223424]

3. Szanda I, Mackewn J, Patay G, et al. National electrical manufacturers association NU-4 performance evaluation of the PET component of the NanoPET/CT preclinical PET/CT scanner. Journal of Nuclear Medicine. 2011; 52:1741–1747. [PubMed: 21969357]

4. Wong WH, Li HD, Baghaei H, et al. Engineering and performance (NEMA and animal) of a lower-cost higher-resolution animal PET/CT Scanner using photomultiplier-quadrant-sharing detectors. Journal of Nuclear Medicine. 2012; 53:1786–1793. [PubMed: 22997277]

5. Larobina M, Brunetti A, Salvatore M. Small animal PET: A review of commercially available imaging systems. Current Medical Imaging Reviews. 2006; 2:187–192.

6. Lewellen TK. Recent developments in PET detector technology. Physics in Medicine and Biology. 2008; 53:R287–R317. [PubMed: 18695301]

7. Eriksson L, Wienhard K, Eriksson M, et al. The ECAT HRRT: NEMA NEC evaluation of the HRRT system, the new high-resolution research tomograph. IEEE Transactions on Nuclear Science. 2002; 49:2085–2088.

8. Stickel JR, Cherry SR. High-resolution PET detector design: modelling compnents of intrinsic spatial resolution. Physics in Medicine and Biology. 2005; 50:179–195. [PubMed: 15742938]

9. Cherry SR. The 2006 Henry N.Wagner lecture: Of mice and men (and positrons) - Advances in PET imaging technology. Journal of Nuclear Medicine. 2006; 47:1735–1745. [PubMed: 17079804]

10. Tai YC, Laforest R. Instrumentation aspects of animal PET. Annual Review of Biomedical Engineering. 2005; 7:255–285.

11. Peng H, Levin CS. Recent developments in PET instrumentation. Current Pharmaceutical Biotechnology. 2010; 11:555–571. [PubMed: 20497121]

12. Espana S, Marcinkowski R, Keereman V, Vandenberghe S, Van Holen R. DigiPET: sub-millimeter spatial resolution small-animal PET imaging using thin monolithic scintillators. Physics in Medicine and Biology. 2014; 59:3405–3420. [PubMed: 24888974]

13. Yamamoto S, Watabe H, Kanai Y, Watabe T, Kato K, Hatazawa J. Development of an ultrahigh resolution Si-PM based PET system for small animals. Physics in Medicine and Biology. 2013; 58:7875–7888. [PubMed: 24145308]

14. Moses WW. Fundamental limits of spatial resolution in PET. Nuclear Instruments & Methods in Physics Research Section a-Accelerators Spectrometers Detectors and Associated Equipment. 2011; 648:S236–S240.

15. Yang YF, Dokhale PA, Silverman RW, et al. Depth of interaction resolution measurements for a high resolution PET detector using position sensitive avalanche photodiodes. Physics in Medicine and Biology. 2006; 51:2131–2142. [PubMed: 16625031]

16. Yang YF, St James S, Wu YB, et al. Tapered LSO arrays for small animal PET. Physics in Medicine and Biology. 2011; 56:139–153. [PubMed: 21119228]

17. St James S, Yang YF, Wu YB, et al. Experimental characterization and system simulations of depth of interaction PET detectors using 0.5 mm and 0.7 mm LSO arrays. Physics in Medicine and Biology. 2009; 54:4605–4619. [PubMed: 19567945]

18. Shah KS, Grazioso R, Farrell R, et al. Position sensitive APDs for small animal PET imaging. IEEE Transactions on Nuclear Science. 2004; 51:91–95.

19. Yang YF, Wu YB, Farrell R, Dokhale PA, Shah KS, Cherry SR. Signal and noise properties of position-sensitive avalanche photodiodes. Physics in Medicine and Biology. 2011; 56:6327–6336. [PubMed: 21896961]

20. Wu Y, Catana C, Cherry SR. A multiplexer design for position-sensitive avalanche photodiode detectors in a PET scanner. IEEE Transactions on Nuclear Science. 2008; 55:463–468.

21. Judenhofer MS, Pichler BJ, Cherry SR. Evaluation of high performance data acquisition boards for simultaneous sampling of fast signals from PET detectors. Physics in Medicine and Biology. 2005; 50:29–44. [PubMed: 15715420]

22. Ren SL, Yang YF, Cherry SR. Effects of reflector and crystal surface on the performance of a depth-encoding PET detector with dual-ended readout. Medical Physics. 2014; 41:072503, 1–9. [PubMed: 24989406]

23. Jan S, Santin G, Strul D, et al. GATE: a simulation toolkit for PET and SPECT. Physics in Medicine and Biology. 2004; 49:4543–4561. [PubMed: 15552416]

24. Siddon RL. Fast calculation of the EXACT radiological path for a 3-dimensional CT array. Medical Physics. 1985; 12:252–255. [PubMed: 4000088]

25. Johnson CA, Yan YC, Carson RE, Martino RL, Daubewitherspoon ME. A system for the 3D reconstruction of retracted-septa PET data using the EM algorithm. IEEE Transactions on Nuclear Science. 1995; 42:1223–1227.

26. Reader AJ, Julyan PJ, Williams H, Hastings DL, Zweit J. EM algorithm system modeling by image-space techniques for PET reconstruction. IEEE Transactions on Nuclear Science. 2003; 50:1392–1397.

27. Bai B, Li Q, Holdsworth CH, et al. Model-based normalization for iterative 3D PET image reconstruction. Physics in Medicine and Biology. 2002; 47:2773–2784. [PubMed: 12200938]

28. NEMA. NEMA Standards Publication NU 4-2008, Performance Measurements of Small Animal Positron Emission Tomography. 2008

29. Catana C, Wu YB, Judenhofer MS, Qi JY, Pichler BJ, Cherry SR. Simultaneous acquisition of multislice PET and MR images: Initial results with a MR-compatible PET scanner. Journal of Nuclear Medicine. 2006; 47:1968–1976. [PubMed: 17138739]

30. Yang YF, Wu YB, Qi J, et al. A prototype PET scanner with DOI-encoding detectors. Journal of Nuclear Medicine. 2008; 49:1132–1140. [PubMed: 18552140]

31. Wu YB, Ng TSC, Yang YF, Shah K, Farrell R, Cherry SR. A study of the timing properties of position-sensitive avalanche photodiodes. Physics in Medicine and Biology. 2009; 54:5155–5172. [PubMed: 19671971]
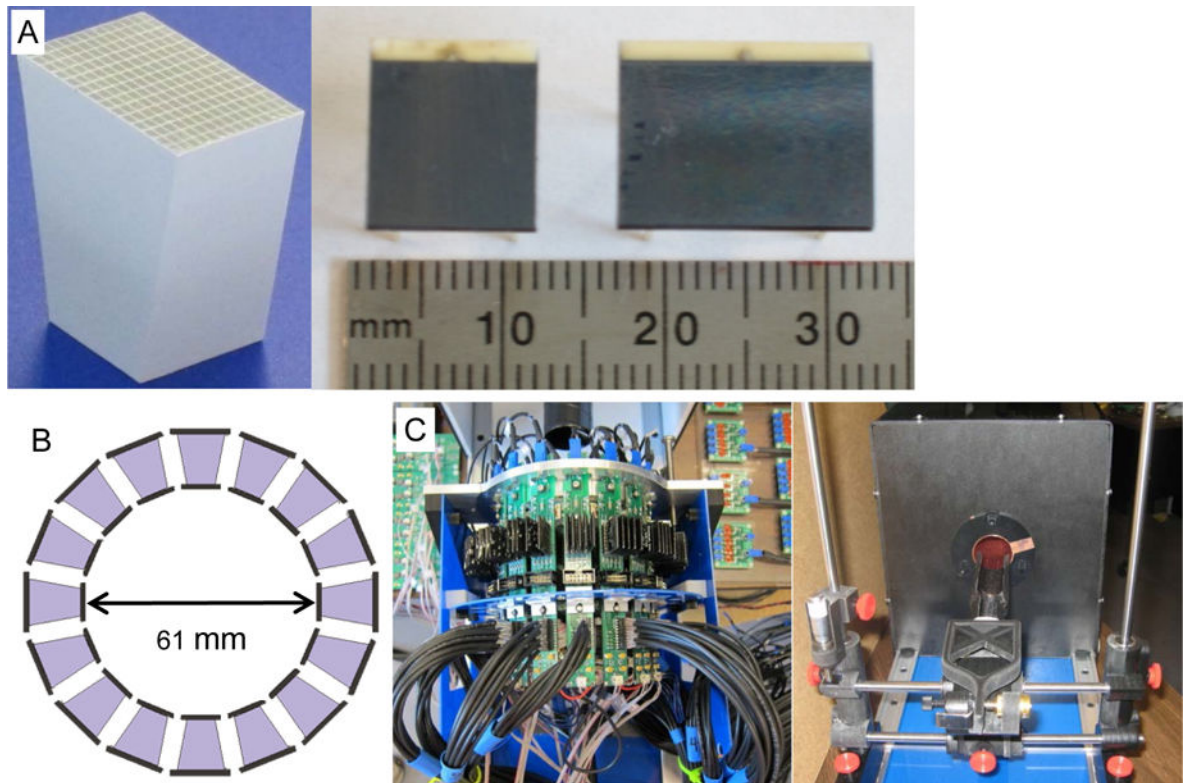
Figure 1.
(A) Tapered LSO array and two different-sized PSAPDs used in the prototype scanner, (B) scale drawing of the prototype 1-ring scanner, (C) photographs of the scanner without the cover showing the readout electronics (left) and, the completed scanner with animal bed (right).
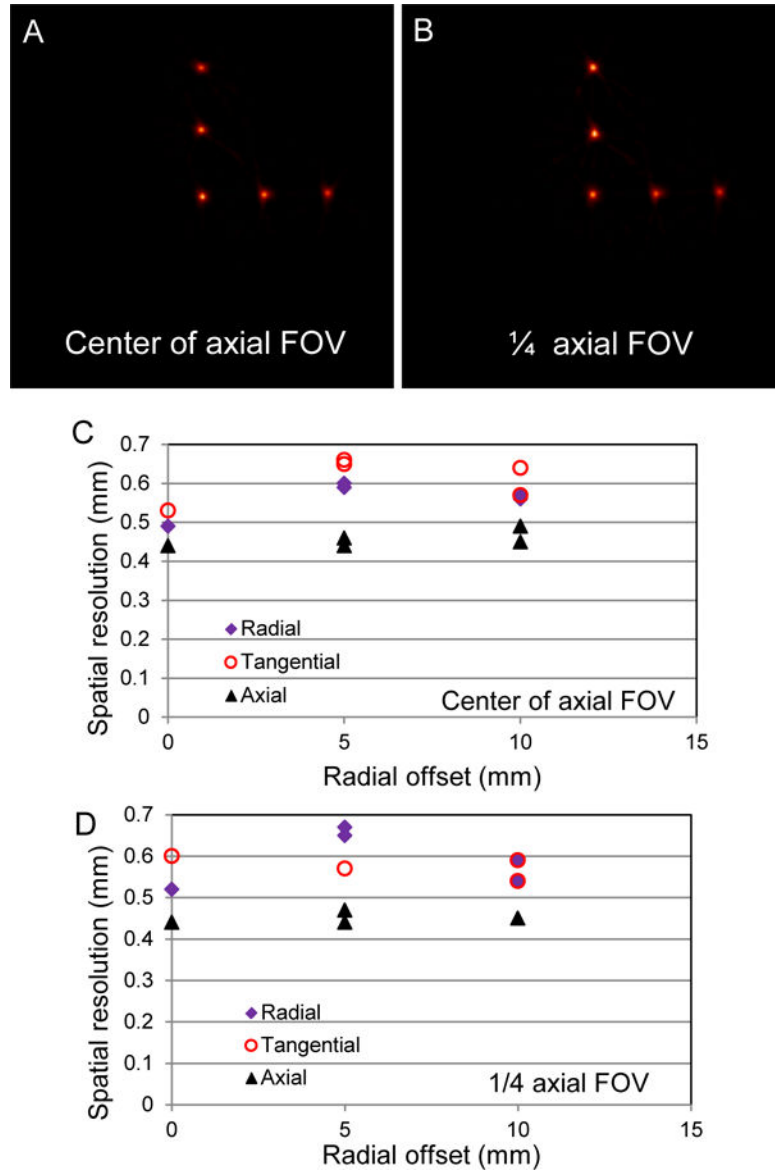
Figure 2.
Reconstructed images from point source measurements. The radial offsets of the point source were 0, 5 and 10 mm. Measurements were made at two different axial locations, (A) in the center of the scanner axially, and (B)1.75 mm away from the central slice. The spatial resolution of the scanner at (C) the center of the axial field of view and (D) in a slice at ¼ axial FOV (1.75 mm from center). Two source positions were measured for radial offsets of 5 and 10 mm as shown in Figure 2A and 2B, therefore there are two data points at these locations.
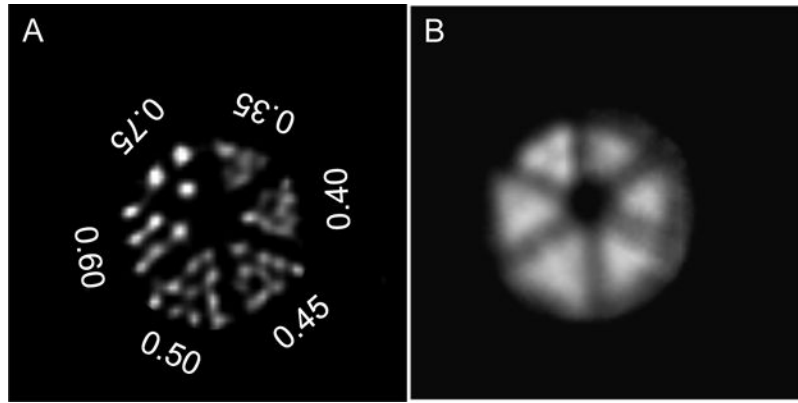
Figure 3.
Reconstructed images of a hot rod phantom obtained from the prototype scanner (A) and the Siemens Inveon D-PET scanner (B).
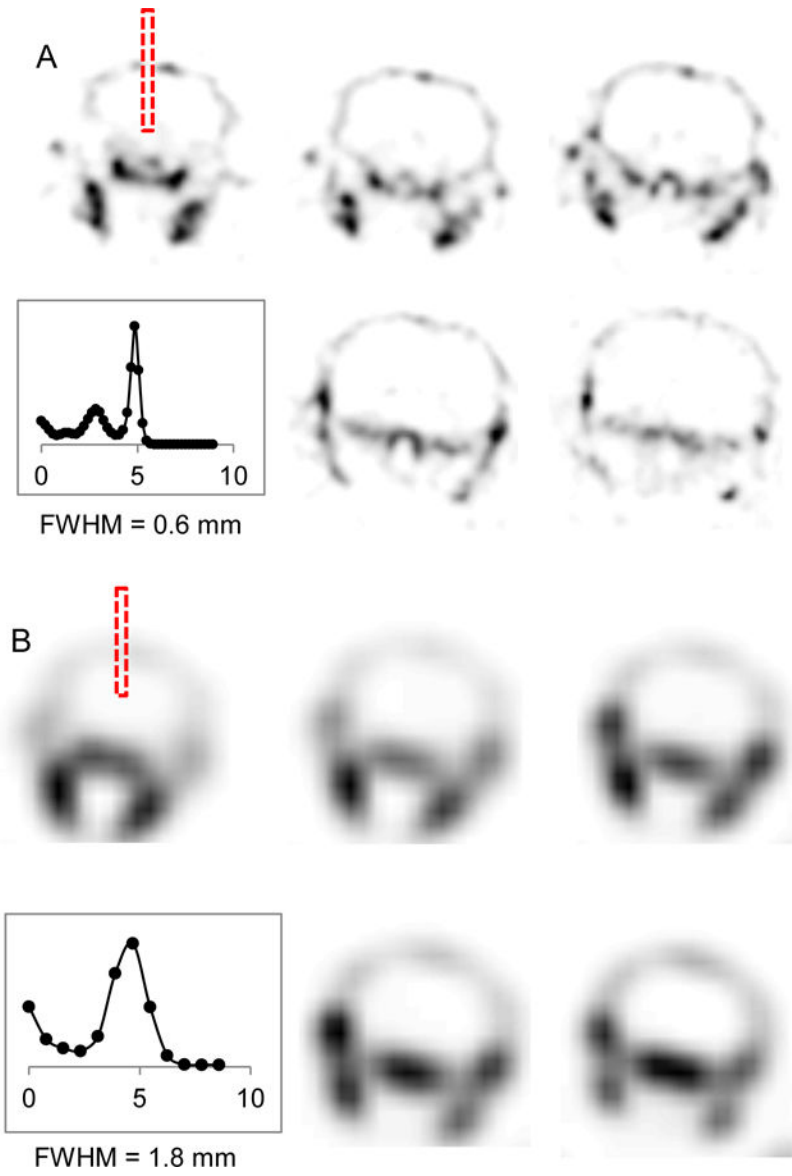
Figure 4.
Reconstructed images of ^{18}F-fluoride uptake in the mouse skull obtained (A) from the prototype scanner and (B) from the Siemens Inveon D-PET scanner. Line profiles through the skull in the first slice of the images are also shown.
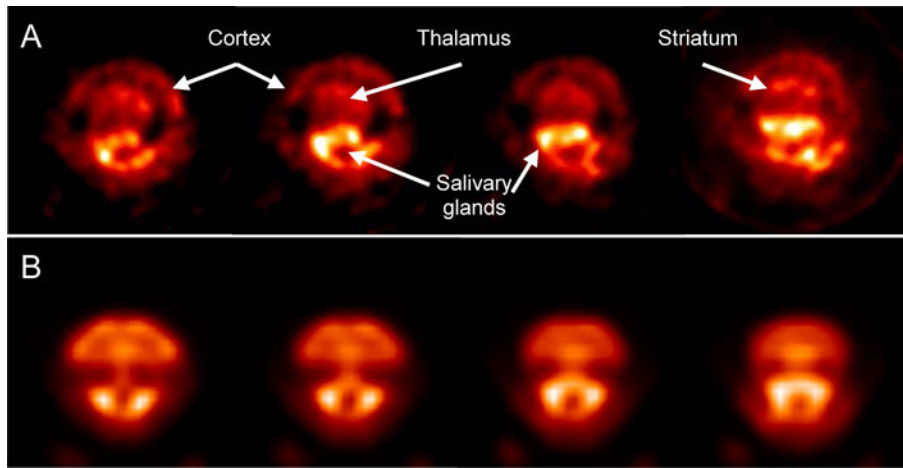
Figure 5.
FDG brain images of a mouse obtained from the prototype scanner (A) and from the Siemens Inveon D-PET scanner (B).